

# *Chandra* Observation of a Group of Galaxies HCG80: Does the Spiral-Only Group Have Hot Intragroup Gas?

Naomi OTA<sup>1</sup>, Umeyo MORITA<sup>2</sup>, Tetsu KITAYAMA<sup>3</sup>, and Takaya OHASHI<sup>2</sup>

<sup>1</sup>*Cosmic Radiation Laboratory, RIKEN, 2-1 Hirosawa, Wako, Saitama 351-0198*

*ota@crab.riken.jp*

<sup>2</sup>*Department of Physics, Tokyo Metropolitan University, 1-1 Minami-osawa, Hachioji, Tokyo 192-0397*

<sup>3</sup>*Department of Physics, Toho University, Funabashi, Chiba 274-8510*

(Received 2004 July 21; accepted 2004 August 22)

## Abstract

We present an analysis of the *Chandra* X-ray observation of a compact group of galaxies HCG80 ( $z = 0.03$ ). The system is a spiral-only group composed of four late-type galaxies and has a high velocity dispersion of  $309 \text{ km s}^{-1}$ . With the high sensitivity *Chandra* observation, we searched for the diffuse X-ray emission from the intragroup medium (IGM), however, no significant emission was detected. We place a severe upper limit on the luminosity of the diffuse gas as  $L_X < 6 \times 10^{40} \text{ erg s}^{-1}$ . On the other hand, significant emission from three of the four members were detected. In particular, we discovered a huge halo emission from HCG80a that extends on a scale of  $\sim 30 \text{ kpc}$  perpendicular to the galactic disk, whose X-ray temperature and luminosity are measured to be  $\sim 0.6 \text{ keV}$  and  $5.6 \times 10^{40} \text{ erg s}^{-1}$  in the 0.5–2 keV band, respectively. It is most likely to be an outflow powered by the intense starburst activity. Based on the results, we discuss possible reasons for the absence of diffuse X-ray emission in the HCG80 group, suggesting the system is subject to the galaxy interactions and possibly at the early stage of the IGM evolution.

**Key words:** galaxies: clusters: individual (HCG80) – galaxies: spiral – X-rays: galaxies – X-rays: ISM

## 1. Introduction

The majority of galaxies are found to reside in groups of galaxies (Tully 1987) and the intragroup medium may dominate the total baryon density of the local universe (Fukugita, Hogan, & Peebles 1998). Groups of galaxies should thus provide useful probes of structure formation in the universe, yet their physical nature is still highly unclear (see Hickson 1997 and Mulchaey 2000 for reviews). The detections of extended X-ray emission have at least shown that a number of groups are gravitationally bound. The observed X-ray luminosities and the inferred gas mass, however, exhibit correlations with gas temperature and galaxy velocity dispersion, much steeper than those predicted from a simple self-similar model (Mulchaey et al. 1996; Ponman et al. 1996). The X-ray emission also tends to be suppressed in spiral-dominated groups (Osmond & Ponman 2004), with a possible exception of HCG57 from which Fukazawa et al. (2002) detected extended thermal emission with *ASCA*. Despite large observational errors, these facts are likely to indicate a close link between galaxy evolution and the properties of the intragroup medium.

Among the 109 galaxy groups observed with the *ROSAT* PSPC, extended X-ray emission is detected in at least 61 groups. No diffuse emission was detected in 12 groups with only spiral members (Mulchaey et al. 2003). Recently the GEMS project constructed a large sample containing 60 groups based on the optical and the *ROSAT* PSPC catalogues (Osmond & Ponman 2004). The X-

ray emission was detected for three of the five spiral-only groups; however, due to the the limited quality of the data, the origin of the emission was not directly constrained but classified into hot halos of the individual galaxies based on their threshold in the spatial extent of  $< 60 \text{ kpc}$ . They suggested based on the anti-correlation between the spiral fraction and the X-ray luminosity that the presence of detectable hot diffuse gas is strongly related to the galaxy morphology. The possible absence of diffuse X-rays in the spiral-only groups would thus imply that either the bound group should contain at least one early-type galaxy, or the X-ray emission is preferentially suppressed in the spiral-only groups for some reason.

To further explore the nature of the diffuse emission from the groups of galaxies, higher quality X-ray data are required. In particular, the high spatial resolution is crucial to separate the emission associated with individual galaxies from the diffuse component. The *Chandra* and *XMM-Newton* are the most suitable satellites for this purpose, yet there have been few observational results available so far. Belsole et al. (2003) recently reported the detection of diffuse X-ray emission from HCG16 ( $z = 0.013$ ) with the *XMM-Newton* EPIC cameras. The temperature and the luminosity were measured to be  $0.49 \pm 0.17 \text{ keV}$  and  $5.0 \times 10^{40} h_{70}^{-2} \text{ erg s}^{-1}$ , respectively. The result obeys the  $L_X - T$  relation obtained for the brighter galaxy groups though it is located at the extreme faint end, from which they suggested that HCG16 is a bound system.

In this paper, we present a *Chandra* observation of a spiral-only group of galaxies, HCG80. This group has

been one of the most plausible candidates, among the known spiral-only groups, for the positive detection of diffuse X-rays for the following reasons. (1) The high line-of-sight velocity dispersion of  $\sigma_v = 309 \text{ km s}^{-1}$  implies the large gravitational potential; accordingly high X-ray luminosity and temperature of  $L_X \sim 8.4 \times 10^{41} h_{70}^{-2} \text{ erg s}^{-1}$  and  $kT \sim 0.8 \text{ keV}$  are expected from the  $\sigma_v - L_X$  and  $\sigma_v - T$  correlations (Ponman et al. 1996). The expected luminosity is close to the  $3\sigma$  upper limit from the previous *ROSAT* PSPC  $L_X = 7.6 \times 10^{41} h_{70}^{-2} \text{ erg s}^{-1}$  (Ponman et al. 1996). (2) Compact galaxy distribution (4 members within  $1'.7$  diameter) has led to a judgment that the HCG80 galaxies are accordant members (Arp 1997; Sulentic 1997). (3) Two of the galaxies are classified as Im, which may indicate the galaxy-galaxy interaction in the group.

In addition, previous observations suggested a causal link between the starburst activity and the galaxy interactions (see Kennicutt 1998 for reviews). Thus the detailed spatial analysis of individual galaxies with an arc-second resolution of *Chandra* is a vital clue to constrain the connection between the outflowing gas and the intragroup medium without suffering from the contamination of point sources. The *Chandra* observations revealed X-ray views of the extended halo emission from the nearby starburst and normal galaxies in the dense environment. For example, the nature of diffuse X-ray emission from NGC253 and NGC55, both of which belong to the nearby spiral-only group, the Sculptor group, are separately studied in Strickland et al. (2002) and Oshima (2003). They exhibit observational evidence for the galactic outflow from the spirals powered by star-formation activity. Strickland et al. (2004a); Strickland et al. (2004b) studied ten star-forming disk galaxies with the *Chandra* X-ray and  $\text{H}\alpha$  imaging data and from the correlations between a variety of X-ray quantities with multi-wavelength data, they quantitatively investigated supernova feedback on the galactic scales.

Through such detailed studies on spiral galaxies we expect to get a new insight into the galaxy-IGM connection. The previous *ROSAT* observations showed that the groups of galaxies have the steeper luminosity-temperature relation compared to clusters of galaxies, which is noticeable for low temperature ( $kT \lesssim 1 \text{ keV}$ ) systems. The preheating effect is suggested to be responsible for the steepening (e.g. Ponman et al. 1996) and Helsdon & Ponman (2003) proposed that spiral galaxies play a comparable role to early types in the gas heating. However it is still ambiguous and to clarify it further investigations are needed.

This paper is organized as follows. In the next section, we describe the *Chandra* observation of a galaxy group HCG80 and the source detection in the field. In section 3, we present the spatial and spectral analyses of HCG80 member galaxies and also constrain the diffuse X-ray emission from the hot intragroup gas. In section 4, we discuss the properties of the member galaxies and in particular the nature of the extended halo emission discovered in the brightest member of the group. We then discuss possible reasons for the absence of the strong X-ray emission from the intragroup gas of HCG80.

Throughout the paper we adopt  $\Omega_M = 0.3$ ,  $\Omega_\Lambda = 0.7$  and  $h_{70} \equiv H_0 / (70 \text{ km s}^{-1} \text{ Mpc}^{-1}) = 1$ , and  $1'$  corresponds to  $36.1 \text{ kpc}$  at  $z = 0.0299$ . Quoted errors indicate the 90% confidence range unless otherwise stated. We use the solar abundance ratio of Anders & Grevesse (1989).

## 2. Observation and source detection

### 2.1. *Chandra* observation of HCG80

The group of galaxies HCG80 consists of four late-type galaxies, HCG80a–d, as shown in Table 1 and Figure 1. Their optical properties are also summarized in the table. We observed HCG80 with the *Chandra* Advanced CCD Imaging Spectrometer (ACIS-S) detector on August 18, 2003 (PI: N. Ota). The pointing coordinates are  $15^{\text{h}}59^{\text{m}}12^{\text{s}}30$ ,  $+65^{\text{d}}24'33''00$  (J2000) and the target was offset from the ACIS-S nominal aim point with a Y-offset of  $-1'$ . The CCD temperature was  $-120^\circ\text{C}$ . The data reduction was performed using CIAO version 3.0.2 with CALDB version 2.25. We analyzed the light curve to find that there is no period of a high background level exceeding  $3\sigma$  above the mean quiescent background rates. Thus the net exposure time is 19712 sec. We did not find any astrometry offset for the data. Since the data was taken with the VFaint mode, the particle background was reduced by screening out events with significant flux in border pixels of the  $5 \times 5$  event islands.

### 2.2. Source detection in the ACIS-S3 Field

We searched for X-ray sources in the ACIS-S3 field of view with the wadedetect algorithm with a significance parameter of  $10^{-6}$  utilizing the 0.3–10 keV band image and detected 20 in total including HCG80a and HCG80b. We also found significant X-ray emission from a direction of HCG80c. The counting rates of four member galaxies are summarized in Table 2. In the following analysis the detected point sources were excluded with a radius of 7 times the size of the Point Spread Function (PSF) which is defined as the 40% encircled energy radius at 1.5 keV at the source position.

The X-ray maximum positions of HCG80a and b in the ACIS-S3 image are  $15^{\text{h}}59^{\text{m}}18^{\text{s}}9$ ,  $+65^{\text{d}}13'57''3$  and  $15^{\text{h}}59^{\text{m}}21^{\text{s}}6$ ,  $+65^{\text{d}}13'22''8$ , respectively. Comparing these with the optical coordinates from Hickson, Kindl, & Auman (1989), they are consistent within  $\lesssim 1''$ . However, due to the limited photon statistics of the present X-ray data, there are uncertainties in the X-ray positions of the galaxies. We thus assume the optical positions from Hickson, Kindl, & Auman (1989) as their centers in our analysis.

## 3. Analysis and results

We analyze X-ray emission from the individual galaxies in section 3.1, 3.2 and 3.3. In section 3.4 we exclude them from the group region and constrain the X-ray emission from the hot intragroup gas.

**Table 1.** Optical properties of member galaxies

Object	Optical coords. (J2000)*		$z$	Diameters <sup>†</sup>	B <sup>‡</sup>	Type
	RA	Dec.				
HCG80	15 <sup>h</sup> 59 <sup>m</sup> 12 <sup>s</sup> .4	+65 <sup>d</sup> 13′33″.3	0.02990			Group
HCG80a	15 <sup>h</sup> 59 <sup>m</sup> 19 <sup>s</sup> .0	+65 <sup>d</sup> 13′57″.4	0.02994	50.8 × 10.8	15.66	Sd
HCG80b	15 <sup>h</sup> 59 <sup>m</sup> 21 <sup>s</sup> .5	+65 <sup>d</sup> 13′22″.7	0.03197	20.4 × 17.4	16.37	Sa
HCG80c	15 <sup>h</sup> 59 <sup>m</sup> 07 <sup>s</sup> .3	+65 <sup>d</sup> 14′00″.8	0.03186	19.6 × 16.4	16.06	Im
HCG80d	15 <sup>h</sup> 59 <sup>m</sup> 12 <sup>s</sup> .1	+65 <sup>d</sup> 13′19″.3	0.03038	27.2 × 10.8	17.01	Im

\* Optical coordinates of the object from Hickson, Kindl, & Auman (1989). <sup>†</sup> Major axis [arcsec] × minor axis [arcsec].  
<sup>‡</sup> B magnitude.

**Table 2.** X-ray count rates, fluxes, and hardness ratios for member galaxies

	$R_{\text{spec}}^*$	$R_{\text{max}}^\dagger$	Soft band		Hard band		$HR^{**}$
			$S^\ddagger$	$f_{\text{X,S}}^\S$	$H^\parallel$	$f_{\text{X,H}}^\#$	
HCG80a	25	31	65.9 ± 6.4	3.4 ± 0.3	5.8 ± 3.5	0.7 ± 0.4	0.09 ± 0.05
HCG80a, nucleus	–	2	14.7 ± 2.7	0.7 ± 0.1	3.5 ± 1.3	0.6 ± 0.2	0.24 ± 0.10
HCG80a, disk+halo	–	31 – 2	50.3 ± 5.8	2.6 ± 0.3	2.9 (< 6.1)	0.3 (< 0.7)	0.06 ± 0.06
HCG80b, nucleus	1.5	2	107.0 ± 7.4	5.3 ± 0.4	34.9 ± 4.2	6.2 ± 0.7	0.33 ± 0.05
HCG80b, disk	–	10 – 2	6.2 ± 1.9	0.2 ± 0.1	0.4 (< 1.4)	0.04 (< 0.15)	0.06 (< 0.23)
HCG80c	–	9.8	5.6 ± 1.9	0.2 ± 0.07	0.3 (< 1.3)	0.04 (< 0.15)	0.06 (< 0.24)
HCG80d	–	13.6	1.7 (< 3.2)	0.06 ± 0.05	< 2.7	< 0.05	1.6 ± 1.4

\* The spectral extraction radius in arcsec (see section 3.3). <sup>†</sup> The maximum radius in arcsec used to estimate the counting rate,  $S$  and  $H$ , and the hardness ratio,  $HR$ . <sup>‡</sup> The X-ray counting rate in the 0.5–2 keV band,  $S$  [ $10^{-4}$  countss $^{-1}$ ]. <sup>§</sup> The X-ray flux in the 0.5–2 keV band,  $f_{\text{X,S}}$  [ $10^{-14}$  ergs $^{-1}$ cm $^{-2}$ ]. <sup>||</sup> The X-ray counting rate in the 2–7 keV band,  $H$  [ $10^{-4}$  countss $^{-1}$ ]. <sup>#</sup> The X-ray flux in the 2–7 keV band,  $f_{\text{X,H}}$  [ $10^{-14}$  ergs $^{-1}$ cm $^{-2}$ ]. <sup>\*\*</sup> The hardness ratio,  $HR = H/S$ . The quoted errors are the  $1\sigma$ .

### 3.1. X-ray morphologies of member galaxies

As shown in Table 2, HCG80a and b are detected with more than  $10\sigma$  significance, we perform detailed analysis of the surface brightness distributions and energy spectra for those two galaxies. As the significance of the X-ray emission from HCG80c and d are low ( $2.6\sigma$  and  $\lesssim 2\sigma$  in the soft band, respectively), we can only measure the fluxes (and luminosities under the assumptions of the spectral models). The results of the flux estimations for the four member galaxies are also presented in Table 2.

In order to constrain the spatial distribution of the X-ray emission from HCG80 a and b, we investigated the surface brightness distribution in two different ways: (1) the radial profile fitting and (2) the 1-dimensional profile fitting. In the former analysis we compare the X-ray radial profile with the simulated PSF to constrain the emission from a nuclear source and the presence of diffuse emission. Since we find a significant extended emission particularly from HCG80a, we study the spatial distribution in detail in the latter analysis. We corrected the positional dependence of the telescope and the detector responses with the exposure maps.

In the case of (1), we produced the soft (0.5–2 keV) and hard (2–7 keV) band images and calculated the radially averaged surface brightness distributions centered at HCG80a and b, as shown in Figure 2. We fitted them separately with the PSF models, which were created by the

HRMA PSF simulator, ChaRT, with specifying the locations of the sources and the spectral models derived from the spectral analysis (section 3.3). The PSF models was generated with sufficient photons so that the statistical uncertainty should be less than 10%, thus negligible compared to the Poisson error of the present data. We investigated the positional dependence of the background intensity using both the blank-sky data and the present data, to find that the background can be regarded as constant within the statistical errors. The background intensities were then estimated from the  $84'' < r < 160''$  ring region of the present pointing data to be  $(4.73 \pm 0.20) \times 10^{-7}$  counts s $^{-1}$  arcsec $^{-2}$  and  $(5.31 \pm 0.21) \times 10^{-7}$  counts s $^{-1}$  arcsec $^{-2}$  in the soft and hard bands, respectively (the errors are  $1\sigma$ ), and included as fixed constants in the fits.

#### HCG80a

For HCG80a, there is clearly an extended emission particularly in the soft energy band in comparison with the PSF (Figure 2a). We then evaluate the emission using the Gaussian functions to find that the single-component Gaussian model can not sufficiently fit the data, suggesting at least two components are necessary to describe the data. Thus in Figure 2a, we show the best-fit model consisting of the PSF and two Gaussians, where the diffuse emission is seen out to the maximum radius of  $R_{\text{max}} \sim 31''$  above the  $2\sigma$  background level. We will analyze the significance of the emission components and the properties

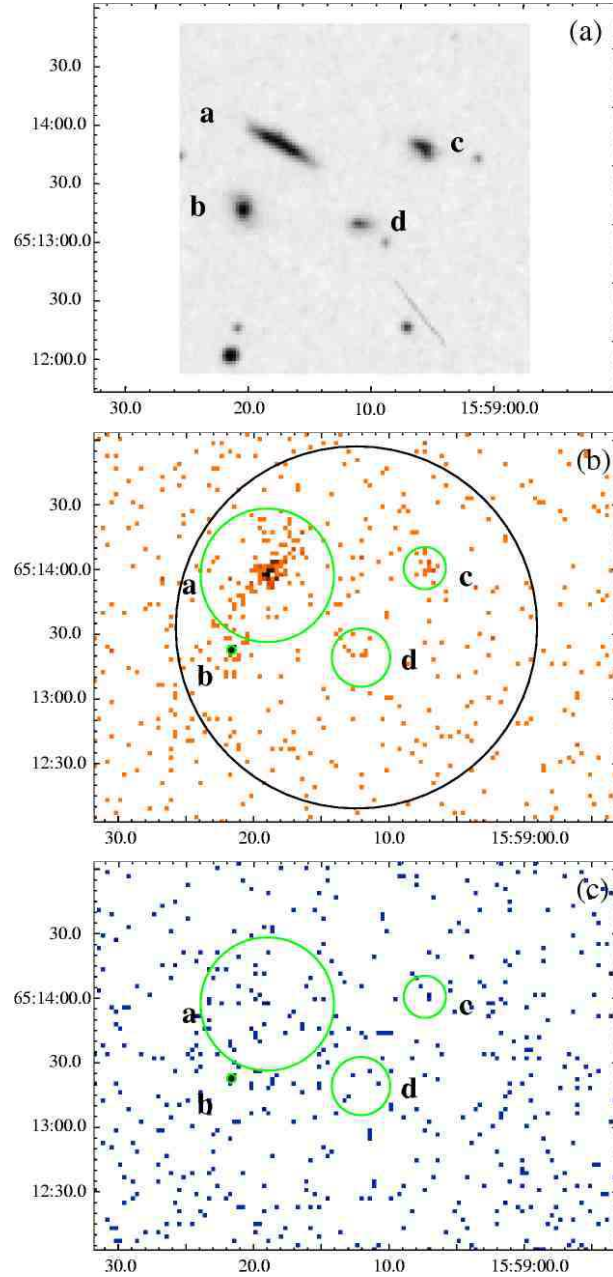


**Fig. 1.** Optical and X-ray images of the spiral-only group, HCG80. In the panel (a), the DSS image of the HCG80 group is shown, where the four members are denoted with a–d. In the panels (b) and (c), the *Chandra* X-ray images in the 0.5–2 keV and 2–7 keV bands are shown. The X-ray images are not smoothed, and background inclusive. The image pixel size is  $2'' \times 2''$ . The member galaxies HCG80a–d are marked with green circles of radii  $r = 31'', 2'', 9'', 13''.6$ , respectively. In the panel (b), the black color represents pixels with the X-ray surface brightness higher than 10 photons per image pixel. The group region used to constrain the diffuse emission in section 3.4 is shown with the circle of radius  $84''$ .

in more detail later.

In the hard energy band, there is excess emission over the background within  $2''$  from the HCG80a optical center. The 2–7 keV counting rate is  $(3.5 \pm 1.3) \times 10^{-4}$  counts  $s^{-1}$ . Under the current statistics, we could not constrain the spatial distribution. However, taking into account the spectral hardness inferred from the analysis in section 3.2 and the nuclear activity reported by Shimada et al. (2000), we suggest that the hard emission may be attributed to

the central AGN in HCG80a.

In the next step, we study the soft diffuse emission from HCG80a, by the 1-dimensional profile fitting. Since the galaxy has a nearly edge-on inclination of  $i = 86^\circ$  following Rubin et al. (1982) (see also Nishiura et al. 2000), the emission from the halo region is expected to be clearly resolved. From Figure 1b we find that the emission extends nearly along the perpendicular direction from the galactic disk of HCG80a whose position angle is  $64^\circ$  (Shimada et

al. 2000). We thus extracted the 1D surface brightness profile along the minor axis of the galaxy, accumulated within  $|r| < 24''$  of the major axis (Figure 3a). The minor-axis profile was rebinned by a factor of 6, then each bin is  $3''$ . We carried out the  $\chi^2$  fitting with some simple models consisting of the Gaussian components for the diffuse emission and the PSF for the central emission whose centers are fixed at the HCG80a center position. As a result, either the single Gaussian or the PSF model cannot provide an acceptable fit, however, adding another Gaussian component, the fit was significantly improved at the 95% level by the F-test. We show the results for the cases of Model 1 (Eq.1) and Model 2 (Eq.2) in table 3.

$$\Sigma_X = \Sigma_{\text{PSF}} + \Sigma_{G1,0} e^{-(y-y_0)^2/\sigma_{G1}^2}, \quad (1)$$

$$\Sigma_X = \Sigma_{G1,0} e^{-(y-y_0)^2/\sigma_{G1}^2} + \Sigma_{G2,0} e^{-(y-y_0)^2/\sigma_{G2}^2}, \quad (2)$$

$$\Sigma_X = \Sigma_{\text{PSF}} + \Sigma_{G1,0} e^{-(y-y_0)^2/\sigma_{G1}^2} + \Sigma_{G2,0} e^{-(y-y_0)^2/\sigma_{G2}^2} \quad (3)$$

where  $y_0$  is fixed at the center of HCG80a and we assume  $\sigma_{G1} < \sigma_{G2}$ . We also fit the profile with Model 3 (Eq.3) and examine the significance of the emission from the central point source. Although the low photon statistics in the central emission resulted in no significant improvement over Model 2 in the F-test at the 95% confidence, we will adopt Model 3 in the rest of our analysis regarding the presence of the optically identified AGN (Shimada et al. 2000) and the observed high hardness ratio in section 3.2.

From the fitting with Model 3, the width for the narrow Gaussian component is obtained to be  $\sigma_{G1} = 3_{-1}^{+2}$  arcsec ( $= 1.8_{-0.6}^{+1.2}$  kpc), which is well consistent with the optical scale of the galactic disk. The broad Gaussian component has a width of  $\sigma_{G2} = 12_{-4}^{+6}$  arcsec ( $= 7.2_{-0.2}^{+0.4}$  kpc) and thus largely extends in comparison to the disk scale. Accordingly we refer to the narrow and the broad Gaussian components respectively as the “disk” and “halo” components hereafter. The extent of the halo emission detected above the  $2\sigma$  background level is  $-26'' < y < 26''$ , corresponding to 31.2 kpc in total. The origin of this huge X-ray halo will be discussed in section 4.

We estimated the luminosity of each component assuming the MEKAL model with an average temperature of 0.56 keV for the disk and the halo, and the power-law model with  $\Gamma = 2.0$  for the nucleus. Here the same definitions as Strickland et al. (2004a) are used to define the emission regions for the nuclear (N), disk (D) and halo(H) components. Namely the luminosities,  $L_{X,N}$ ,  $L_{X,D}$ , and  $L_{X,H}$  are accumulated from the  $r < 1$  kpc circle, a rectangular aperture oriented along the minor axis of major-axis length 28.9 kpc and extending between  $-2 \text{ kpc} < y < 2 \text{ kpc}$ , and a  $28.9 \text{ kpc} \times 39.1 \text{ kpc}$  rectangular aperture oriented along the minor axis with excluding the N and D regions. We obtain  $L_{X,D} = 2.2 \times 10^{40} \text{ erg s}^{-1}$ ,  $L_{X,H} = 3.8 \times 10^{40} \text{ erg s}^{-1}$ , and  $L_{X,N} = 1.7 \times 10^{40} \text{ erg s}^{-1}$  in the 0.5–2 keV, respectively. The results are also shown in Table 5.

We also notice that the intensity of the halo emission from the Northern hemisphere is stronger than the Southern one by a factor of  $\sim 2.7 \pm 2.1$  if we fit the

Northern and Southern halos separately with Model 3 with fixing the model parameters except for  $\Sigma_{G2,0}$  at the best-fit values derived in the above analysis. Thus there may be some asymmetry. However because the the current statistics is limited, we could not further constrain the spatial distribution of the halo emission.

We show the major-axis profile accumulated within  $|y| < 5''$  of the minor axis in Figure 3b. It can be fitted by the Gaussian with  $\sigma = 4 \pm 1$  arcsec ( $= 2.4 \pm 0.6$  kpc) and the normalization for the central surface brightness of  $108_{-27}^{+49} \times 10^{-9} \text{ photons s}^{-1} \text{ cm}^{-2} \text{ arcsec}^{-2}$ . We found that the width is close to that of the narrow component in Model 3, namely  $\sigma \sim \sigma_{G1}$ . Thus the disk emission is concentrated within about  $3''.5$  from the center while we did not find significant emission extending over the optical scale of the galactic disk.

### HCG80b

From the comparison to the simulated PSFs, we found that the innermost data points of the radial surface brightness distributions are well consistent with the PSFs in both the soft and the hard energy bands, and the resultant  $\chi^2$  values of 24.6 and 34.4 for 20 degrees of freedom. However we find there are systematic residuals over the PSFs in several consecutive bins around  $r \sim 10''$ , which can be attributed to the extra emission around the point source. Because the emission is found within a radius roughly corresponding to the size of the optical disk  $\sim 10''$ , we refer to it as the disk component while to the central point source as the nucleus component hereafter. The photon counts coming from the disk component in a radius range of  $2'' < r < 10''$  are  $12 \pm 4$  and  $< 3$ , in the soft and hard bands, respectively (see also Table 2).

In order to further constrain the emission profile, we attempt to fit the 0.5–7 keV radial profile with the PSF plus Gaussian model, as shown in Figure 2. This provides an acceptable fit with  $\chi^2/\text{dof} = 19.3/18$  and the PSF intensity is obtained as  $(1.13 \pm 0.17) \times 10^{-5} \text{ photons s}^{-1} \text{ cm}^{-2}$  and the Gaussian normalization and the width are  $3.5_{-2.6}^{+3.5} \times 10^{-9} \text{ photons s}^{-1} \text{ cm}^{-2} \text{ arcsec}^{-2}$  and  $12_{-5}^{+7}$  arcsec ( $= 7_{-3}^{+4}$  kpc), respectively. Because the model parameters are associated with large uncertainties, the emission profile particularly for the diffuse emission is not well constrained, which we consider is due to the low signal to noise ratios at the outer radius. Therefore we decide to fix the maximum radius at the size of the optical disk,  $R_{\text{max}} = 10''$  when evaluating the X-ray intensities for the disk emission. While within  $2''$  from the HCG80b peak, the central nuclear component dominates the total emission, we use the maximum radius of  $R_{\text{max}} = 2''$  for the HCG80b nucleus. The luminosities of the nucleus ( $r < 2''$ ) and the disk ( $2'' < r < 10''$ ) are estimated to be  $(2.9 \pm 0.2) \times 10^{41} \text{ erg s}^{-1}$  and  $(5.8 \pm 1.8) \times 10^{39} \text{ erg s}^{-1}$  in the 0.5–7 keV assuming the power-law model with  $\Gamma = 1.9$  (see section 3.3) and the MEKAL model with  $kT = 0.5$  keV and  $Z = 0.1$  solar, respectively.

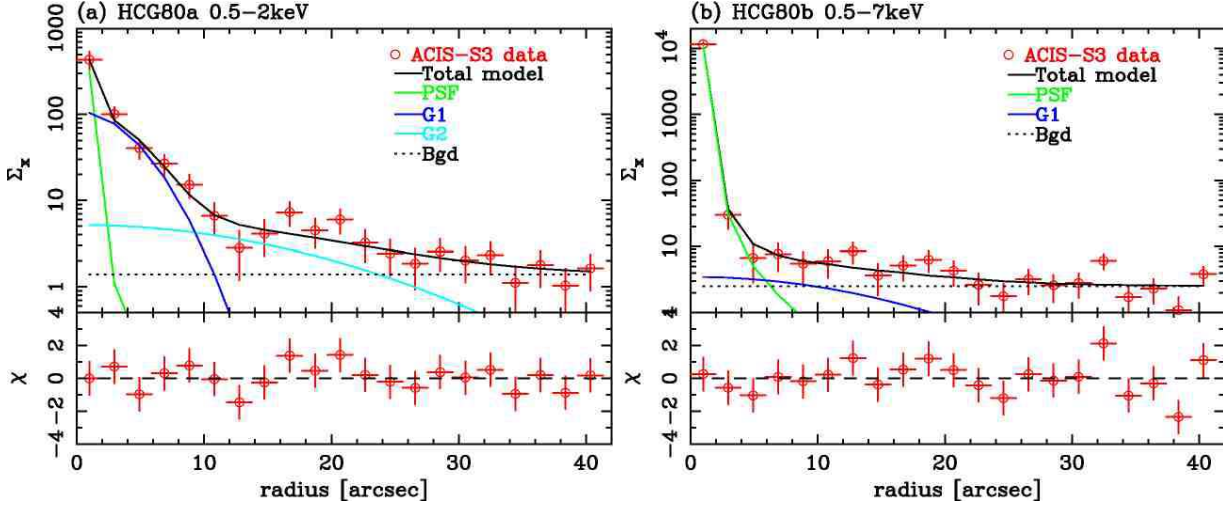


**Fig. 2.** Radial profile fitting for HCG80a and b with the PSF and Gaussian(s) models. In the panels (a) and (b), the ACIS-S3 radial surface brightness distribution for HCG80a in the 0.5–2 keV and HCG80b in the 0.5–7 keV are shown with red crosses. The best-fit total model is shown with the black solid line in each panel, where the PSF and Gaussian components representing the disk and halo emissions are also indicated with the green, blue and light-blue lines. The background intensity is shown with the horizontal dotted line. In the upper panels  $\Sigma_X$  is in the units of  $10^{-9}$  photons  $s^{-1} \text{cm}^{-2} \text{arcsec}^{-2}$  while in the bottom panels the residuals of the fits are shown in the units of  $\sigma$ .

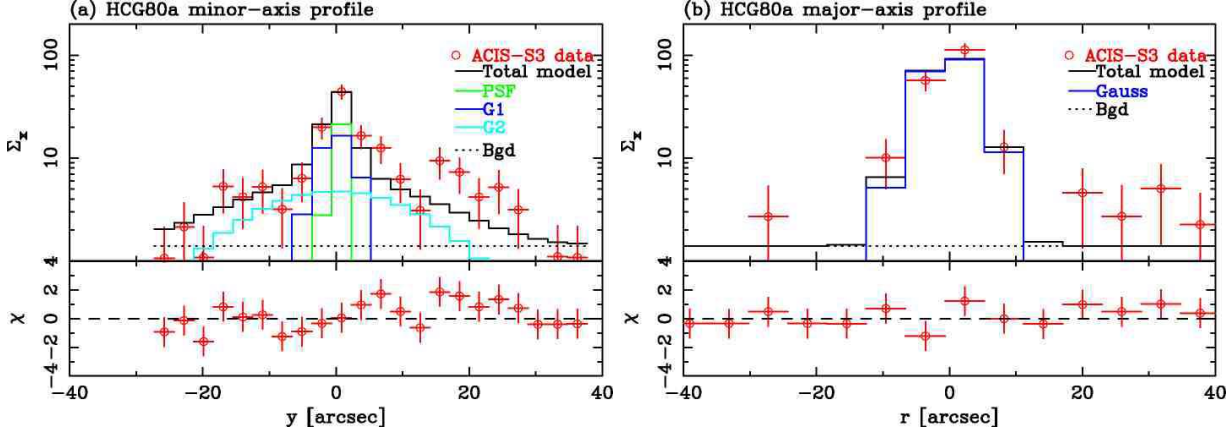


**Fig. 3.** Minor-axis and major-axis X-ray surface brightness distributions. In the panels (a) and (b), the crosses denote the observed 1-dimensional surface brightness profiles accumulated within  $|r| < 24''$  of the major axis and  $|y| < 5''$  of the minor axis in the soft band, respectively. The surface brightness,  $\Sigma_X$  is in the units of  $10^{-9}$  photons  $s^{-1} \text{cm}^{-2} \text{arcsec}^{-2}$ . In the panel (a), the solid line shows the result of the fitting with Model 3. The PSF, narrow Gaussian, broad Gaussian, and background components are indicated with the dashed, dash-dot, dash-dot-dot-dot, dot lines, respectively. In the panel (b), the solid and dotted lines show the best-fit Gaussian and the background constant, respectively.

### 3.2. Hardness ratio analysis

To provide a quantitative evaluation of the spatial variation of the X-ray spectra, the hardness ratios for the central and the surrounding disk (+ halo) regions are shown in Table 2. We define the hardness ratio as  $HR \equiv H/S$ , where  $S$  and  $H$  are the photon counts in the 0.5–2 and 2–7 keV bands, respectively. Due to the low significance of the emission from HCG80c and d, we show the values derived for the entire galaxy regions for these two galaxies. There is an indication that the HCG80a central emission ( $r < 2''$ ) is hard compared with the outer ( $2'' < r < 31''$ ) region. If we simply assume the spectra

being described by the power-law (or the  $Z = 0.1$  solar MEKAL) model attenuated by the Galactic absorption, the power-law indices (or the gas temperature) for the nucleus and the disk + halo regions of HCG80a correspond to  $\Gamma = 2.2 \pm 0.4$  ( $kT = 2.6 \pm 1.4$  keV) and  $\Gamma = 3.5 (> 2.8)$  ( $kT = 1.0 (< 1.4)$  keV), respectively. While the HCG80b nucleus region ( $r < 2''$ ) shows a large  $HR$  value, corresponding to the power-law index of  $1.9 \pm 0.2$ , the  $HR$  for the outer, disk region ( $2'' < r < 10''$ ) was not constrained. In the next subsection we explore the spectra from the HCG80a “nucleus + disk + halo” and the HCG80b “nucleus” regions by the thermal and/or non-thermal spectral modeling to constrain their origins.

**Table 3.** Results of the 1D fitting for HCG80a in the soft band

Parameter	Model 1	Model 2	Model 3
	PSF+G1	G1+G2	PSF+G1+G2
PSF [photons s <sup>-1</sup> cm <sup>-2</sup> ]	43 <sup>+13</sup> <sub>-14</sub> × 10 <sup>-9</sup>	–	25(< 45) × 10 <sup>-9</sup>
Σ <sub>G1,0</sub> [photons s <sup>-1</sup> cm <sup>-2</sup> arcsec <sup>-2</sup> ]	7.6 <sup>+5.2</sup> <sub>-2.8</sub> × 10 <sup>-9</sup>	36.4 <sup>+19.5</sup> <sub>-12.6</sub> × 10 <sup>-9</sup>	17.2 <sup>+31.7</sup> <sub>-12.4</sub> × 10 <sup>-9</sup>
σ <sub>G1</sub> [arcsec]	10 ± 4	2 ± 1	3 <sup>+2</sup> <sub>-1</sub>
Σ <sub>G2,0</sub> [photons s <sup>-1</sup> cm <sup>-2</sup> arcsec <sup>-2</sup> ]	–	5.6 <sup>+3.8</sup> <sub>-2.8</sub> × 10 <sup>-9</sup>	4.7 <sup>+3.5</sup> <sub>-2.8</sub> × 10 <sup>-9</sup>
σ <sub>G2</sub> [arcsec]	–	12 <sup>+6</sup> <sub>-4</sub>	12 <sup>+6</sup> <sub>-4</sub>
χ <sup>2</sup> /dof	26.2/19	22.7/18	20.6/17

Strickland et al. (2004a) suggested, based on the *Chandra* data for ten star-forming galaxies, that the disk emission tends to be harder than the halo emission however we did not find any meaningful HR variation between the two regions in HCG80a due to the poor photon statistics of the present data.

### 3.3. X-ray spectra of member galaxies

We extracted X-ray spectra for HCG80a and b from circular regions with radii  $R_{\text{spec}} = 25''$  and  $1''.5$ , respectively (Figure 4). Note that  $R_{\text{spec}}$  was chosen so that about 90% of the X-ray photons from each galaxy are accumulated as well as that there is no overlapping area between the two galaxies. We fitted the spectra with the power-law model and the MEKAL thin-thermal plasma model (Mewe et al. 1985; Mewe et al. 1986; Kaastra 1992; Liedahl et al. 1995). The absorption column density was fixed at the Galactic value,  $N_{\text{H}} = 2.5 \times 10^{20} \text{ cm}^{-2}$  (Dickey & Lockman 1990).

#### HCG80a

For HCG80a, the power-law spectral model is rejected at the 99% confidence level. On the other hand, the MEKAL model provides a good fit to the data with the  $\chi^2$  value of 5.9 for 5 degree of freedom. We obtained the temperature and the metallicity to be  $0.59^{+0.12}_{-0.10}$  keV and  $0.07^{+0.18}_{-0.05}$  solar, respectively. Though the AGN emission is estimated to be only  $\sim 20\%$  of the total emission from the image analysis, we checked whether the temperature determination of the intragroup gas is influenced by the AGN component in the following two ways: (1) exclude the central  $r < 5''$  circular region from the HCG80a overall spectrum and fit it with the MEKAL model, and (2) fit the overall spectrum with the two-component model, where the power-law index and the metallicity are respectively fixed at 2.0 and 0.1 solar. We found that both two analyses yielded the consistent temperatures ( $\sim 0.6$  keV) within the errors, thus we show the results for the case (2) in Table 4. We also confirmed that the ratio of the X-ray luminosities between the AGN and the diffuse components is consistent with the result of the image analysis under Model 3 within 10%.

#### HCG80b

We found that the HCG80b spectrum can be fitted either by the power-law model and the MEKAL model. Even though the MEKAL temperature of  $kT \sim 3.5$  keV

may be consistent with a collection of Low Mass X-ray Binaries, the observed luminosity of  $2.6 \times 10^{41} \text{ erg s}^{-1}$  is by more than 3 orders higher than the values for normal spiral galaxies. On the other hand, the power-law index of  $\Gamma = 1.94^{+0.19}_{-0.18}$  deduced from the X-ray spectral fitting is consistent with values of known AGNs. We also estimated the  $\alpha_{\text{OX}}$  index, which is a slope of a hypothetical power law connecting the B band and 2 keV, to be 1.9. The value is larger in comparison to the result of the *ROSAT* large quasar survey but within a scatter of the quasars (Figure 2 of Green et al. 1995). Thus the emission from the central  $r < 1''.5$  region is most likely to be originating from the AGN in the galaxy.

### 3.4. Constraints on the hot diffuse emission

In order to constrain the X-ray emission from the hot intragroup medium, we define the group region with the  $r = 84'' = 50.5$  kpc circle whose center is the same as that of HCG80,  $15^{\text{h}}59^{\text{m}}12^{\text{s}}.4, +65^{\text{d}}13'33''.3$  (Hickson, Kindl, & Auman 1989), which encompasses the optical disks of the four member galaxies (Figure 1b). We subtracted the background and the galaxy contributions from the total photon counts in the group region and derive the intensity of the intragroup emission. Note that we used the background intensity estimated from the outer ring region. The source counts within  $31''$  from the brightest member, HCG80a is estimated based on the results of the image analysis presented in section 3.1, while for HCG80b–d, the observed source counts within circles of radii  $R_{\text{max}} = 10''$ ,  $9''.8$  and  $13''.6$ , which approximately equal to the sizes of the optical disks, are used.

Subtracting the galaxy contributions,  $130 \pm 12$ ,  $223 \pm 15$ ,  $11 \pm 3$ ,  $3(< 5)$  counts for HCG80a–d and the background,  $213 \pm 9$  counts from the total photon counts of  $576 \pm 24$  in the group region, we found that there is no significant emission from the hot IGM and the  $3\sigma$  upper limit is obtained to be 92 photons in the 0.5–2 keV band. We also confirmed that the present estimation on the IGM emission is not affected by the choice of the extraction radii,  $R_{\text{max}}$  for the galaxies b–d; if we change  $R_{\text{max}}$  by a factor of 0.5 – 1.5, the result changes by only  $\lesssim 10\%$ . If further assuming the temperature and the metallicity of the gas to be comparable to those derived for HCG16,  $kT \sim 0.5$  keV and  $Z \sim 0.1$  solar (Belsole et al. 2003), the bolometric luminosity is constrained as  $L_X < 6.3 \times 10^{40} \text{ erg s}^{-1}$  ( $3\sigma$ ). We show a location of HCG80 on the  $L_X - f_{\text{spiral}}$  plane in Figure 5.

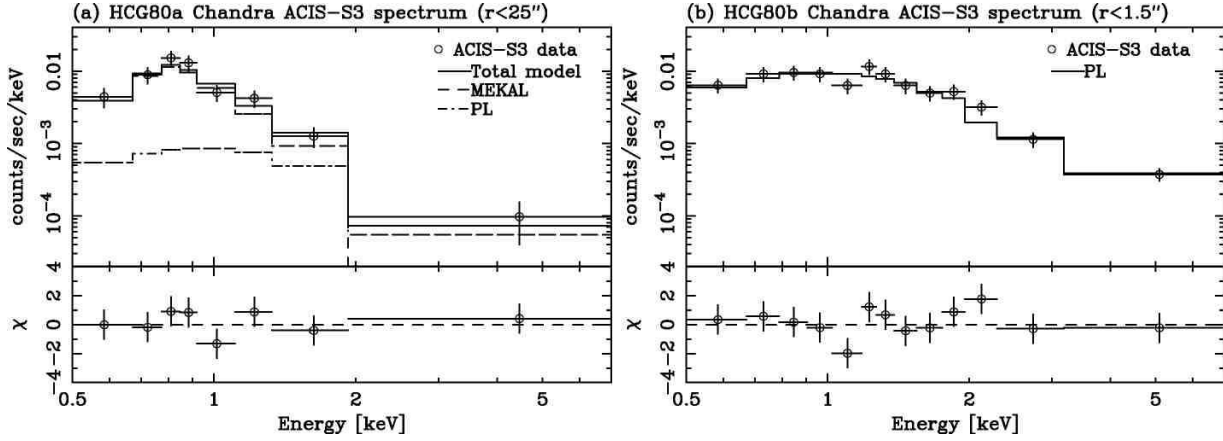


Fig. 4. *Chandra* ACIS-S3 spectra of HCG80a (a) and HCG80b (b). In the upper panes, the open circles denote the observed spectra and the step functions show the best-fit spectral models (the MEKAL+Power-law model for HCG80a and the Power-law model for HCG80b) convolved with the telescope and the detector response functions. In the lower panels, the residuals of the fit are shown.

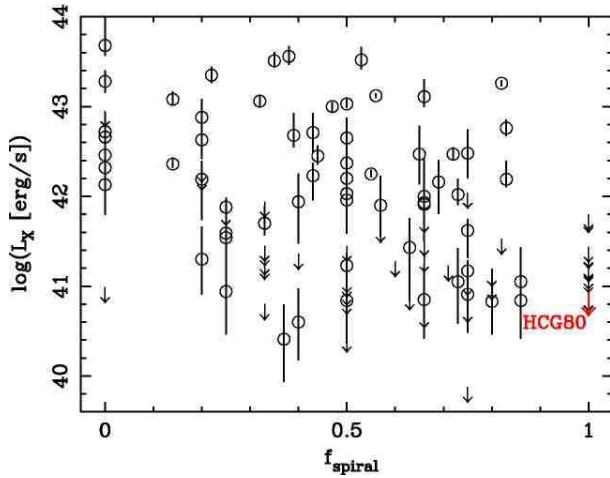


Fig. 5.  $L_X - f_{\text{spiral}}$  relation. The groups with constrained/unconstrained bolometric luminosity from the *ROSAT* PSPC survey (Mulchaey et al. 2003) are plotted with open circle/arrow, as a function of the spiral fraction. The upper limit on the bolometric luminosity for the hot diffuse gas in HCG80 obtained from the present *Chandra* analysis is shown with the red arrow.

## 4. Discussion

From the high-resolution *Chandra* observation of the spiral-only group HCG80, we detected significant X-ray emission from three of the four member galaxies, HCG80a, b, and c and investigated the spatial distribution and the spectral features for HCG80a and b in detail. In particular we discovered the halo emission from HCG80a, which extends  $\sim 30$  kpc perpendicular to the galactic disk. We will compare the X-ray luminosity of the member galaxies to those of optical in section 4.1, and further discuss the origin of the halo emission from HCG80a in section 4.2. On the other hand, we found that there is not any significant emission from the group region. The absence of strong X-ray emission will be discussed in section 4.3

### 4.1. X-ray properties of the member galaxies

We show the relation between the bolometric X-ray luminosity,  $L_X$ , and the B band luminosity,  $L_B$ , for the HCG80 members in Figure 6. In addition to the overall luminosities of the galaxies, the luminosities of the nucleus, disk and halo regions are separately plotted for HCG80a and b. The X-ray luminosities were estimated from the spectral analysis for HCG80a and the HCG80b nucleus. However because the spectra for the HCG80b disk, HCG80c and d were not constrained, we assume the thermal emission with  $kT = 0.5$  keV and  $Z = 0.1$  solar to convert the photon counting rates in the soft band (Table 2) to  $L_X$ . The assumption may be valid because the hardness ratios listed in Table 2 are in agreement with the values for the soft thermal emission.

Comparing to the best-fit  $L_X - L_B$  relation for the late-type galaxies in the Helsdon et al. (2001) sample, we found that the disk component of HCG80b and the overall luminosities of HCG80c and d are consistent with their relation if taking into account the measurement errors and the large data scatter among the other late-type galaxies. On the other hand, HCG80a and b clearly show higher  $L_X$  value than expected from the  $L_X - L_B$  relation from Helsdon et al. (2001). They noted that the galaxies associated with the AGN and/or the starburst activities tend to lie above the best-fitting line, namely they have enhanced X-ray emission relative to the optical. Thus considering from the thermal nature of the extended emission of HCG80a and the hard spectrum of the point-like emission from HCG80b found in the previous section, the higher  $L_X$  values agree with their indication.

Furthermore, the starburst galaxies are often identified on the basis of their high IR luminosity and warm FIR colors,  $f_{60}/f_{100} > 0.4$ . The FIR fluxes are available only for HCG80a. From the IRAS 12-, 25-, 60- and 100- $\mu\text{m}$  fluxes,  $(f_{12}, f_{25}, f_{60}, f_{100}) = (0.10, 0.16, 2.31, 5.16)$  Jy, the IR luminosity is  $L_{\text{IR}} = 12.3 \times 10^{10} L_{\odot}$  utilizing  $L_{\text{IR}} = 5.67 \times 10^5 D_{\text{Mpc}}^2 (13.48 f_{12} + 5.16 f_{25} + 2.58 f_{60} + f_{100}) L_{\odot}$  (Sanders & Mirabel 1996). This is consistent with the  $L_X -$



**Table 4.** Results of the spectral fitting for HCG80a and HCG80b

Galaxy	Model	Parameter	Value (90% error)	$\chi^2/\text{dof}$
HCG80a ( $R_{\text{spec}} = 25''$ )	MEKAL	$kT$ [keV]	$0.59^{+0.12}_{-0.10}$	
		$Z$ [solar]	$0.07^{+0.18}_{-0.05}$	
		$z$	0.02994 (F)	
		$k_M^*$	$9.9^{+8.3}_{-5.7} \times 10^{-5}$	5.9/5
	PL +MEKAL	$\Gamma$	2.0 (F)	
		$k_P^\dagger$	$< 5.2 \times 10^{-6}$	
		$kT$ [keV]	$0.56^{+0.12}_{-0.17}$	
		$Z$ [solar]	0.1 (F)	
		$z$	0.02994 (F)	
		$k_M^*$	$7.4^{+2.9}_{-1.9} \times 10^{-5}$	4.4/5
		$f_{X,P}$ [erg s $^{-1}$ cm $^{-2}$ ] $^\ddagger$	$< 2.1 \times 10^{-14}$	
		$L_{X,P}$ [erg s $^{-1}$ ] $^\ddagger$	$< 4.6 \times 10^{40}$	
		$L_{\text{bol},P}$ [erg s $^{-1}$ ] $^\ddagger$	$< 6.1 \times 10^{40}$	
		$f_{X,M}$ [erg s $^{-1}$ cm $^{-2}$ ] $^\S$	$(2.8 \pm 0.5) \times 10^{-14}$	
		$L_{X,M}$ [erg s $^{-1}$ ] $^\S$	$6.5^{+0.8}_{-1.2} \times 10^{40}$	
$L_{\text{bol},M}$ [erg s $^{-1}$ ] $^\S$	$7.8^{+1.2}_{-1.6} \times 10^{40}$			
HCG80b ( $R_{\text{spec}} = 1''.5$ )	PL	$\Gamma$	$1.94^{+0.19}_{-0.18}$	
		$k_P^\dagger$	$2.5^{+0.3}_{-0.3} \times 10^{-5}$	10.7/11
		$f_{X,P}$ [erg s $^{-1}$ cm $^{-2}$ ] $^\ddagger$	$10.6^{+1.6}_{-1.8} \times 10^{-14}$	
		$L_{X,P}$ [erg s $^{-1}$ ] $^\ddagger$	$(2.6 \pm 0.3) \times 10^{41}$	
	MEKAL	$kT$ [keV]	$3.5^{+1.6}_{-1.0}$	
		$Z$ [solar]	$< 0.17$	
		$z$	0.03197 (F)	
		$k_M^*$	$1.07^{+0.16}_{-0.14} \times 10^{-4}$	12.7/10

\* The normalization factor for the MEKAL model,  $k_M = \int n_e n_H dV / 4\pi (D_A (1+z))^2$  [ $10^{-14}$  cm $^{-5}$ ], where  $D_A$  is the angular diameter distance to the source.  $^\dagger$  The normalization factor for the power-law (PL) model,  $k_P$  [photonskeV $^{-1}$ cm $^{-2}$ s $^{-1}$ ] at 1keV. (F) Fixed parameters.  $^\ddagger$  The 0.5–7 keV X-ray flux and the 0.5–7 keV luminosity for the PL model.  $^\S$  The 0.5–7 keV X-ray flux and the 0.5–7 keV luminosity for the MEKAL model.

$L_{\text{IR}}$  correlation for the starburst galaxies (Strickland et al. 2004b; Helsdon et al. 2001).  $f_{60}/f_{100} = 0.45$ ; hence HCG80a is ‘‘FIR warm’’. Thus the above facts strongly support that the X-ray emission from HCG80a is produced by the starburst activity. In the next subsection, we derive some physical parameters to characterize the starburst and compare them to the previous measurements on other starburst galaxies, in the light of energy feedback from massive stars.

#### 4.2. Starburst activity in HCG80a

The huge extraplanar emission discovered in HCG80a reminds us of the bipolar outflow in the bright starburst galaxy such as M82 (e.g. Lehnert, Heckman, & Weaver 1999). The X-ray luminosity from the HCG80a halo is determined to be  $\sim 4 \times 10^{40}$  erg s $^{-1}$  (Table 5), which is even larger than those reported for the bright starburst galaxies. We show a detailed comparison of luminosities derived in section 3.1 and the emission-weighted X-ray temperature to the values reported for M82 and NGC253 (Strickland et al. 2004a). We also show the star formation rate estimated from the IR luminosity,  $\text{SFR}_{\text{IR}} = 21.1 M_\odot \text{yr}^{-1}$ , where  $\text{SFR}_{\text{IR}} = 4.5 \times 10^{-44} L_{\text{IR}}$  [ergs $^{-1}$ ] (Kennicutt 1998).

In order to investigate the physical properties of the X-ray emitting thermal plasma in the halo, we treat the emission region as a cylinder of diameter 4 kpc and height 30 kpc and estimate the electron density and the gas mass. Thus the following values are meaningful as order-of-magnitude estimates only. The volume of the cylinder is  $V = 1.1 \times 10^{67}$  cm $^3$  and the emission integral of the corresponding region is  $EI = n_e n_H V = 1.44 \times 10^{64}$  cm $^{-3}$  based on the result of the spectral fitting. These yielded the electron density, the thermal pressure, the thermal energy and the gas mass for the average temperature of  $T = 6.5 \times 10^6$  K as follows:

$$n_e = 4.0 \times 10^{-2} \text{ cm}^{-3}, \quad (4)$$

$$P_{\text{th}}/k = n_e T = 2.6 \times 10^5 \text{ Kcm}^{-3}, \quad (5)$$

$$M_{\text{gas}} = \mu_e m_p n_e V = 4.3 \times 10^8 M_\odot, \quad (6)$$

$$E_{\text{th}} = \frac{3}{2} (n_e + n_H) k T V = 1.1 \times 10^{57} \text{ ergs}, \quad (7)$$

where we adopt  $n_H = (\mu_e/\mu_H)n_e$ ,  $\mu_e = 1.167$ , and  $\mu_H = 1.40$ . The above values are higher by about a factor of  $\gtrsim 5$  than those obtained for NGC253 (Strickland et al. 2002) if we neglect any systematic error.

The radiative cooling timescale of the gas and the mass

**Table 5.** Halo, disk, nuclear and total luminosities

Galaxy	$\langle kT \rangle^*$	Band <sup>†</sup>	$L_{X,H}^\ddagger$	$L_{X,D}^\S$	$L_{X,N}^\parallel$	$L_{X,tot}^\#$	$L_B^{**}$	$L_{IR}^{**}$	SFR <sub>IR</sub> <sup>††</sup>
HCG80a	$0.56^{+0.12}_{-0.17}$	0.5–2	$3.5 \pm 0.5$	$2.0 \pm 0.4$	$1.6 \pm 0.3$	$7.1 \pm 0.7$	0.75	12.3	21.1
HCG80a	$0.56^{+0.12}_{-0.17}$	0.3–2	$4.5 \pm 0.7$	$2.6 \pm 0.4$	$2.1 \pm 0.4$	$9.2 \pm 0.9$	0.75	12.3	21.1
M82 <sup>‡‡</sup>	0.37	0.3–2	0.41	1.6	2.3	4.3	0.33	5.36	9.2
NGC253 <sup>‡‡</sup>	0.25	0.3–2	0.12	0.33	0.094	0.55	0.58	2.10	3.6

\* The emission-weighted X-ray temperature of the diffuse emission in keV. <sup>†</sup> The energy band in keV used to calculate the X-ray luminosities. <sup>‡,§,||</sup> The X-ray luminosities for the halo (H), the disk (D), and the nucleus (N) regions in  $10^{40} \text{erg s}^{-1}$ . <sup>#</sup> The total X-ray luminosity for the H + D + N regions in  $10^{40} \text{erg s}^{-1}$ . The errors of the luminosity measurements for HCG80a are the  $1\sigma$ . <sup>\*\*</sup> The B and IR luminosities in  $10^{10} L_\odot$ . <sup>††</sup> The star formation rate from the IR luminosity,  $\text{SFR}_{\text{IR}} = 4.5 \times 10^{-44} L_{\text{IR}} [\text{erg s}^{-1}]$  (Kennicutt 1998). <sup>‡‡</sup> The values are taken from Strickland et al. (2004a).

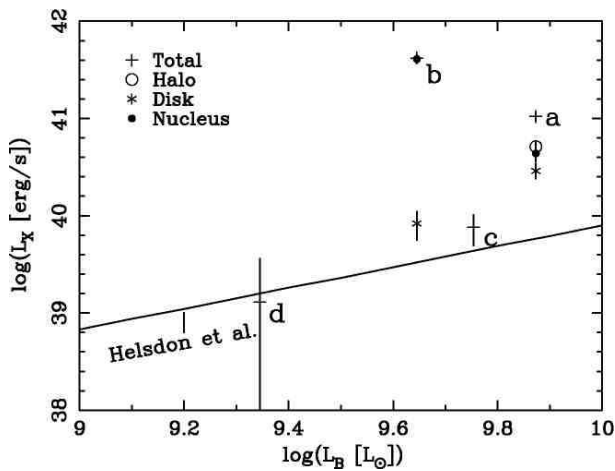


**Fig. 6.**  $L_X - L_B$  relation. The bolometric luminosity of the overall galaxy region is plotted against the B luminosity [ $L_\odot$ ] for each galaxy (cross). For HCG80a, the nucleus, disk and halo components are also separately shown with the solid circle, asterisk, and open circle, respectively. For HCG80b, the nucleus and the disk components are shown with the solid circle and asterisk, respectively. The error bars are the  $1\sigma$ . The solid line represents the best-fit  $L_X - L_B$  relation for the late-type galaxies (Helsdon et al. 2001)

cooling rate are estimated to be  $t_{\text{cool}} \sim E_{\text{th}}/L_{\text{bol}} = 390 \text{ Myr}$  and  $\dot{M}_{\text{gas}} \sim 1.1 M_\odot \text{yr}^{-1}$ . Then supposing that the flow velocity may be approximated by the sound speed of the gas,  $v_{\text{flow}} \sim v_s = 292 \text{ km s}^{-1}$ , the time necessary to travel the distance of 15 kpc (a half of the height of the cylinder) is  $t_{\text{flow}} \sim 50 \text{ Myr}$ . Since  $t_{\text{cool}} \gg t_{\text{flow}}$ , the condition maintaining the halo emission seems to be satisfied.

The above calculations and the high SF rate inferred from the IR luminosity indicate that the enormous thermal energy of  $\sim 10^{57} \text{ erg}$  would be supplied through successive SN explosions and the formation of superbubbles. We will estimate the SN rate and also compare the estimated quantities with the “disk blowout” condition to test a plausibility of the present interpretation.

Assuming the Type II supernova energy input of  $10^{51} \text{ erg}$  and a canonical value for the thermalization efficiency of 10%, the thermal energy contained in the hot gas requires  $\sim 10^7 \text{ SNe}$ . Thus the SN rate is expected to

be  $\sim 10^7/t_{\text{flow}} = 0.2 \text{ yr}^{-1}$  to keep the  $\sim 10^7$  ejecta in the halo region. Alternatively with the IR luminosity and the relation from Heckman, Armus, & Miley (1990), the SN rate is  $R_{\text{SN}} = 0.2 L_{\text{IR}}/10^{11} L_\odot \sim 0.25 \text{ yr}^{-1}$ . Then if the successive star formation had lasted in the past  $t_{\text{SF}} = 40 \text{ Myr}$  and one supernova may supply thermal energy of  $10^{50} \text{ erg s}^{-1}$ , the SN rate of  $0.25 \text{ yr}^{-1}$  can account for the thermal energy in the halo of  $E_{\text{th}} \sim 10^{57} \text{ ergs}$  (Eq. 7). The duration of  $t_{\text{SF}} = 40 \text{ Myr}$  is comparable to the timescale of the outflow  $t_{\text{flow}}$  and seems reasonable also from the point of view of the typical lifetime of massive stars,  $\sim 10 \text{ Myr}$ .

We next consider whether the gas can really escape from the galaxy potential well against the gravitational force. The escape velocity is estimated to be  $v_{\text{esc}} \sim 120 \text{ km s}^{-1}$  (or equivalently  $kT \sim 0.14 \text{ keV}$ ) utilizing the mass-to-light ratio of  $M/L_B \simeq 60h(R/0.1\text{Mpc})M_\odot/L_\odot$  for spiral galaxies (Bahcall, Lubin, & Dorman 1995). Here we assumed the galaxy mass within  $R$  is given by  $M \sim Rv_{\text{esc}}^2/G$  and adopted  $R = 15 \text{ kpc}$ , which corresponds to the isophotal radius,  $R_{25}$  (Hickson 1993). Note that the rotation curve was measured within the central  $r \lesssim 4 \text{ kpc}$  by Nishiura et al. (2000). Though it is difficult to infer  $v_{\text{esc}}$  from their result due to the existence of asymmetry between the approaching and receding sides of the galaxy, the average rotation velocity is roughly  $\sim 130 \text{ km s}^{-1}$  and thus comparable to that estimated above. Therefore the observed temperature of 0.6 keV is sufficiently high for the gas to escape into the intergalactic space.

The critical mechanical luminosity for the disk blowout (see Strickland et al. 2004b and references therein) is calculated as  $L_{\text{crit}} = 4.2 \times 10^{40} \text{ erg s}^{-1}$ . The mechanical energy injection of the halo may be given by  $L_W \sim L_{X,H} = 3.5 \times 10^{40} \text{ erg s}^{-1}$ . Therefore  $L_W \sim L_{\text{crit}}$ . Furthermore, we compare the density of the halo region derived in Eq. 4 to the model calculation of disk-halo interaction by Norman & Ikeuchi (1989) to find that it is within the chimney/starburst phase where the blow-out occurs.

The mass flow rate is estimated to be  $\dot{M}_{\text{flow}} \sim M_{\text{gas}}v_{\text{flow}}/y \sim 8.5 M_\odot \text{yr}^{-1}$ , where  $v_{\text{flow}} = v_s$  and  $y = 15 \text{ kpc}$  are assumed. For the well-known bright starburst galaxies, NGC253 and M82, the rates are  $\dot{M}_{\text{flow}} = 5.8(v_{\text{flow}}/1000 \text{ km s}^{-1})(y/6.35 \text{ kpc})^{-1} M_\odot \text{yr}^{-1}$  (Strickland et al. 2002) and

$12.9(v_{\text{flow}}/600 \text{ kms}^{-1})(y/6 \text{ kpc}) M_{\odot}\text{yr}^{-1}$  (Strickland, Ponman, & Stevens 1997), assuming the volume filling factor of the hot plasma to be 1 and the metal abundance of  $Z=0.05$  solar. Thus the mass flow rate for HCG80a is likely to be one the largest among the other known starburst galaxies. Furthermore, like the cylindrical structure of the CO molecular gas observed in M82 (Nakai et al. 1987), the outflow of cold matter undetectable in X-rays may raise the  $\dot{M}_{\text{flow}}$  value significantly if exists. For example, if the total mass flow is ten times larger than that estimated from the X-ray observation only,  $t_{\text{SF}} = 40 \text{ Myr}$  will result in the total mass loss of  $\sim 4 \times 10^9 M_{\odot}$ . This corresponds to about 10% of the total galaxy mass inferred from the  $M/L_B$  ratio,  $M \sim 4.7 \times 10^{10} M_{\odot}$ .

In conclusion it is highly plausible that HCG80a is a starburst galaxy that exhibits one of the most energetic outflow powered by the starburst activity known in the universe.

#### 4.3. Diffuse hot gas in HCG80

We obtained a severe constraint on the intensity of the diffuse emission from the HCG80 group region,  $L_X < 6.3 \times 10^{40} \text{ erg s}^{-1}$ , which is one of the lowest among the *ROSAT* groups of galaxies (Figure 5). The flux sensitivity of the present *Chandra* observation is higher by a factor of about 25 than that of the previous *ROSAT*/PSPC observation (Ponman et al. 1996). Thus it is clear that the current upper limit is lower by more than one order of magnitude than that expected from the  $\sigma - L_X$  relation. In comparison to the X-ray luminosity of HCG16 measured with *XMM-Newton*,  $L_X = 5.0 \times 10^{40} h_{70}^{-2} \text{ erg s}^{-1}$  (Belsole et al. 2003), our upper limit is comparable to their result. If we further assume that the intragroup gas in HCG80 is a 0.5 keV thermal plasma, distributed within a sphere of radius 50 kpc, the upper limits on the electron density and the total gas mass are estimated to be  $n_e < 8.4 \times 10^{-4} \text{ cm}^{-3}$  and  $M_{\text{IGM}} < 1.3 \times 10^{10} M_{\odot}$ .

Suppose that the HCG80 group is a virialized system and the velocity dispersion properly measures the potential well, the total mass is  $M_{\text{tot}} = 3\sigma_v^2 R/G \sim 3.4 \times 10^{12} M_{\odot}$ , yielding the gas mass to the total mass ratio of  $< 0.004$ . This unusually small value may be a consequence of the following possibilities; 1) HCG80 is a chance alignment and not a real, physical system, 2) HCG80 is a virializing, young system and the gas is yet to be heated to emit appreciable X-rays, or 3) the diffuse gas is expelled from HCG80 by, for instance, a violent activity of member galaxies.

Regarding the first possibility, the differences in the line of sight velocity relative to HCG80a are  $\Delta cz = +621, +587, +145 \text{ km s}^{-1}$  for HCG80b, c, d, respectively (Arp 1997). They satisfy the criterion of  $\Delta cz < 1000 \text{ km s}^{-1}$  for the accordant system applied in Arp (1997). It is admittedly difficult to judge from the  $\Delta cz$  values alone whether galaxies are indeed concentrated compared to the field sample, since the velocity dispersion of the member galaxies,  $309 \text{ km s}^{-1}$  corresponds to the comoving separation of 4.3 Mpc. The four members of HCG80, however,

are clustered within a circle of  $r = 50.5 \text{ kpc}$  on the sky, yielding a cylindrical volume containing the four galaxies of  $0.07 \text{ Mpc}^3$ . This is only 1/15 of the mean occupied volume,  $\sim 1 \text{ Mpc}^3$ , of field galaxies brighter than HCG80d ( $B = 17$ ), based on the luminosity function in the SDSS b<sub>j</sub> band (Blanton et al. 2001). This is supportive of a significant galaxy concentration in the HCG80 group.

We further note that an exceptionally strong activity inferred in HCG80a may be a result of galaxy interaction in the high density environment. Coziol, Brinks, & Bravo-Alfaro (2004) quantified the level of activity (star formation or AGN) using a sample of 91 galaxies in the compact groups and suggested an evolutionary sequence that groups at their early stage of evolution tend to be rich in late-type members with high activity levels and show smaller velocity dispersion. Since our results show that HCG80 contains at least two active galaxies and the velocity dispersion of  $\sigma_v = 309 \text{ km s}^{-1}$  is relatively small among their sample, HCG80 is likely to be close to their configuration “type A” corresponding to a lower level of evolution. In addition, Verdes-Montenegro et al. 2001 showed that the groups richer in early type galaxies or more compact with larger velocity dispersion have a weak tendency to be more deficient in HI gas than expected from the optical luminosities, and proposed a scenario that the amount of HI gas would decrease further with evolution by tidal stripping and/or heating. Therefore no significant HI deficiency in HCG80 may also imply the lower level of evolution. In order to further confirm the reality of the system and constrain the physical properties, it is necessary to identify the distances of the HCG80 galaxies and also search for the evidence of interactions.

As pointed out by Mulchaey (2000), the hypothesis that the all spiral-only group is a mere chance alignment is unlikely given the existence of the our own spiral-only Local Group. We thus compare our result with the Local Group. Wang & McCray (1993) found the soft X-ray component with temperature 0.2 keV in the soft X-ray background, which could due to a warm intragroup medium in the Local Group. Rasmussen et al. (2003) measured the absorption line features towards three AGNs using the *XMM-Newton*/RGS deep spectroscopic data, whose redshift appear to be  $z \sim 0$ , and placed limits on the electron density,  $n_e < 2 \times 10^{-4} \text{ cm}^{-3}$ , the scale length of the absorber,  $L > 140 \text{ kpc}$ , and its mass,  $M_{\text{IGM}} < 5 \times 10^{10} M_{\odot}$  in a collisional equilibrium approximation. Thus the upper limit on the hot IGM in the HCG80 group from the *Chandra* observation is similar to that of the Local Group, suggesting the spiral-only groups may contain very tenuous IGM.

Another interpretation may be possible in the context of the preheating models for groups (e.g. Ponman, Cannon, & Navarro 1999). The model predicts that the energy input through galactic winds or outflows powered by supernovae should cause a more extended gas distribution, resulting the gas density too low to be detected in X-rays. Thus the large halo emission discovered in HCG80a and the low density of the intergalactic medium suggested from the analysis are not in conflict with the view of the

preheating model. However it is inconclusive because the non-detection of the diffuse intragroup gas does not allow us to put any quantitative constraint on a connection between the outflowing gas and the intragroup gas. Future follow-up observations will be meaningful to further clarify the role of late-type galaxies in the evolution of the IGM probably at its early stage.

We are grateful to Y. Ishisaki and T. Oshima for their technical support and useful comments. N.O. acknowledges support from the Special Postdoctoral Researchers Program of RIKEN. U. M. is supported by a Research Fellowship for Young Scientists from the JSPS.

## References

- Anders, E., & Grevesse, N. 1989, *Geochim. Cosmochim. Acta*, 53, 197
- Arp, H. 1997, *ApJ*, 474, 74
- Bahcall, N. A., Lubin, L. M., & Dorman, V. 1995, *ApJL*, 447, L81
- Belsole, E., Sauvageot, J.-L., Ponman, T. J., & Bourdin, H. 2003, *A&A*, 398, 1
- Blanton, M. R., et al. 2001, *AJ*, 121, 2358
- Coziol, R., Brinks, E., & Bravo-Alfaro, H. 2004, *astro-ph/0404066*
- Devereux, N. A. & Eales, S. A. 1989, *ApJ*, 340, 708
- Dickey, J. M., & Lockman, F.J. 1990, *ARA&A*, 28, 215
- Dos Santos, S. & Mamon, G. A. 1999, *A&A*, 352, 1
- Fukazawa, Y., Kawano, N., Ohta, A., & Mizusawa, H. 2002, *PASJ*, 54, 527
- Fukugita, M., Hogan, C. J., & Peebles, P. J. E. 1998, *ApJ*, 503, 518
- Green, P. J., Schartel, N., Anderson, S. F., Hewett, P. C., Foltz, C. B., Brinkmann, W., Fink, H., Trumper, J., Margon, B. 1995, *ApJ*, 450, 51
- Heckman, T. M., Armus, L., & Miley, G. K. 1990, *ApJS*, 74, 833
- Helsdon, S. F. & Ponman, T. J. 2003, *MNRAS*, 340, 485
- Helsdon, S. F., Ponman, T. J., O'Sullivan, E., & Forbes, D. A. 2001, *MNRAS*, 325, 693
- Hickson, P., Kindl, E., & Auman, J. R. 1989, *ApJS*, 70, 687
- Hickson, P. 1993, *Astrophysical Letters Communications*, 29, 1
- Hickson, P. 1997, *ARA&A*, 35, 357
- Kaastra, J. S. 1992, *An X-Ray Spectral Code for Optically Thin Plasmas* (Internal SRON-Leiden Report, updated version 2.0)
- Kennicutt, R. C. 1998, *ARA&A*, 36, 189
- Lehnert, M. D., Heckman, T. M., & Weaver, K. A. 1999, *ApJ*, 523, 575
- Liedahl, D.A., Osterheld, A.L., and Goldstein, W.H. 1995, *ApJ*, 438, L115
- Nakai, N., Hayashi, M., Handa, T., Sofue, Y., Hasegawa, T., & Sasaki, M. 1987, *PASJ*, 39, 685
- Nishiura, S., Shimada, M., Ohyama, Y., Murayama, T., & Taniguchi, Y. 2000, *AJ*, 120, 1691
- Norman, C. A. & Ikeuchi, S. 1989, *ApJ*, 345, 372
- Mewe, R., Gronenschild, E.H.B.M., and van den Oord, G.H.J. 1985, *A&AS*, 62, 197
- Mewe, R., Lemen, J.R., & van den Oord, G.H.J. 1986, *A&AS*, 65, 511
- Mulchaey, J. S., Davis, D. S., Mushotzky, R. F., & Burstein, D. 1996, *ApJ*, 456, 80
- Mulchaey, J. S., Davis, D. S., Mushotzky, R. F., & Burstein, D. 2003, *ApJS*, 145, 39
- Mulchaey, J. S. 2000, *ARA&A*, 38, 289
- Oshima, T. 2003, Ph.D. Thesis, Univ. of Tokyo
- Osmond, J. P. F. & Ponman, T. J. 2004, *MNRAS*, 350, 1511
- Ponman, T. J., Bourner, P. D. J., Ebeling, H., & Bohringer, H. 1996, *MNRAS*, 283, 690
- Ponman, T. J., Cannon, D. B., & Navarro, J. F. 1999, *Nature*, 397, 135
- Rasmussen, A., Kahn, S.M., Paerels, F. 2003, *astro-ph/0301183*
- Ribeiro, A. L. B., de Carvalho, R. R., Capelato, H. V., & Zepf, S. E. 1998, *ApJ*, 497, 72
- Rubin, V. C., Ford, W. K., Thonnard, N., & Burstein, D. 1982, *ApJ*, 261, 439
- Sanders, D. B. & Mirabel, I. F. 1996, *ARA&A*, 34, 749
- Strickland, D. K., Ponman, T. J., & Stevens, I. R. 1997, *A&A*, 320, 378
- Strickland, D. K., Heckman, T. M., Weaver, K. A., Hoopes, C. G., & Dahlem, M. 2002, *ApJ*, 568, 689
- Strickland, D. K., Heckman, T. M., Colbert, E. J. M., Hoopes, C. G., & Weaver, K. A. 2004, *ApJ*, 606, 829
- Strickland, D. K., Heckman, T. M., Colbert, E. J. M., Hoopes, C. G., & Weaver, K. A. 2004, *ApJS*, 151, 193
- Shimada, M., Ohyama, Y., Nishiura, S., Murayama, T., & Taniguchi, Y. 2000, *AJ*, 119, 2664
- Sulentic, J. W. 1997, *ApJ*, 482, 640
- Tully, R. B. 1987, *ApJ*, 323, 1
- Verdes-Montenegro, L., Yun, M. S., Williams, B. A., Huchtmeier, W. K., Del Olmo, A., & Perea, J. 2001, *A&A*, 377, 812
- Wang, Q. D. & McCray, R. 1993, *ApJL*, 409, L37